

The Impact of a 3-D Earth Structure on Glacial Isostatic Adjustment in Southeast Alaska Following the Little Ice Age

Marsman, C. P.; van der Wal, W.; Riva, R. E.M.; Freymueller, J. T.

DOI

[10.1029/2021JB022312](https://doi.org/10.1029/2021JB022312)

Publication date

2021

Document Version

Final published version

Published in

Journal of Geophysical Research: Solid Earth

Citation (APA)

Marsman, C. P., van der Wal, W., Riva, R. E. M., & Freymueller, J. T. (2021). The Impact of a 3-D Earth Structure on Glacial Isostatic Adjustment in Southeast Alaska Following the Little Ice Age. *Journal of Geophysical Research: Solid Earth*, 126(12), Article e2021JB022312. <https://doi.org/10.1029/2021JB022312>

Important note

To cite this publication, please use the final published version (if applicable). Please check the document version above.

Copyright

Other than for strictly personal use, it is not permitted to download, forward or distribute the text or part of it, without the consent of the author(s) and/or copyright holder(s), unless the work is under an open content license such as Creative Commons.

Takedown policy

Please contact us and provide details if you believe this document breaches copyrights. We will remove access to the work immediately and investigate your claim.

JGR Solid Earth



RESEARCH ARTICLE

10.1029/2021JB022312

Key Points:

- The regional 3D upper mantle viscosity structure is constrained using glacial isostatic adjustment, seismic tomography, and mineral physics
- Lateral viscosity variations have no significant impact on the glacial isostatic model predictions in the region
- Non-thermal effects play a dominant role in variations in seismic anomalies in the shallow upper mantle in this region

Supporting Information:

Supporting Information may be found in the online version of this article.

Correspondence to:

C. P. Marsman,
c.p.marsman@uu.nl

Citation:

Marsman, C. P., van der Wal, W., Riva, R. E. M., & Freymueller, J. T. (2021). The impact of a 3-D Earth structure on glacial isostatic adjustment in Southeast Alaska following the Little Ice Age. *Journal of Geophysical Research: Solid Earth*, 126, e2021JB022312. <https://doi.org/10.1029/2021JB022312>

Received 27 APR 2021

Accepted 2 NOV 2021

The Impact of a 3-D Earth Structure on Glacial Isostatic Adjustment in Southeast Alaska Following the Little Ice Age

C. P. Marsman^{1,2,3} , W. van der Wal^{1,2} , R. E. M. Riva¹ , and J. T. Freymueller⁴ 

¹Faculty of Civil Engineering and Geosciences, Delft University of Technology, Delft, The Netherlands, ²Faculty of Aerospace Engineering, Delft University of Technology, Delft, The Netherlands, ³Department of Earth Sciences, Utrecht University, Utrecht, The Netherlands, ⁴Department of Earth and Environmental Sciences, Michigan State University, East Lansing, MI, USA

Abstract In Southeast Alaska, extreme uplift rates are primarily caused by glacial isostatic adjustment (GIA), as a result of ice thickness changes from the Little Ice Age to the present combined with a low-viscosity asthenosphere. Previous GIA models adopted a 1-D Earth structure. However, the actual Earth structure is likely more complex due to the long history of subduction and tectonism and the transition from a continental to an oceanic plate. Seismic evidence indeed shows a laterally heterogeneous Earth structure. In this study, a numerical model is constructed for Southeast Alaska, which allows for the inclusion of lateral viscosity variations. The viscosity follows from scaling relationships between seismic velocity anomalies and viscosity variations. We use this scaling relationship to constrain the thermal effect on seismic variations and investigate the importance of lateral viscosity variations. We find that a thermal contribution to seismic anomalies of 10% is required to explain the GIA observations. This implies that non-thermal effects control seismic anomaly variations in the shallow upper mantle. Due to the regional geologic history, it is likely that hydration of the mantle impact both viscosity and seismic velocity. The best-fit model has a background viscosity of 5.0×10^{19} Pa-s, and viscosities at ~ 80 km depth range from 1.8×10^{19} to 4.5×10^{19} Pa-s. A 1-D averaged version of the 3-D model performed slightly better, however, the two models were statistically equivalent within a 2σ measurement uncertainty. Thus, lateral viscosity variations do not contribute significantly to the uplift rates measured with the current accuracy and distribution of sites.

Plain Language Summary Rapid uplift in Southeast Alaska is caused by past and current melting of glaciers—which is termed “Glacial Isostatic Adjustment” (GIA). Traditionally, GIA models have considered a vertically stratified Earth model. However, the Earth’s structure below Southeast Alaska is more complex and laterally variable due to a long history of subduction and tectonism. We aim to reconstruct the mantle viscosity below Southeast Alaska to best match the present-day GPS observations. Viscosity describes how readily the mantle flows when subjected to forces. We prescribe our models with an ice load history derived from ice-mass changes during and after the Little Ice Age. We test several models that predict the 3D viscosity using seismic velocity models and search for a parameter that determines how much of those variations are caused by temperature as opposed to other effects. We show that, the lateral variations in the Earth do not significantly impact the modeled uplift predictions in comparison to a laterally averaged uniform structure. This may be due to limitations of the seismic model. We find that, the viscosity variations are slightly influenced by thermal effects and are more likely due to hydration of the mantle, which is consistent with the tectonic history of this region.

1. Introduction

In Southeast Alaska, glacial isostatic adjustment (GIA) is the dominant process causing present-day vertical crustal motions. Since the early 2000s, GPS observations have highlighted two major uplift areas centered at the Yakutat (YK) and Glacier Bay (GB) ice fields, exceeding 30 mm/yr (Hu & Freymueller, 2019), as shown in Figure 1. Past studies, beginning with Larsen et al. (2005), have shown that these uplift rates are the result of the Earth’s viscoelastic response to the decline of glaciers after the Little Ice Age (LIA), and elastic rebound to present-day ice melt (PDIM). Raised shorelines indicate that uplift started at the end of

© 2021. The Authors.

This is an open access article under the terms of the [Creative Commons Attribution License](https://creativecommons.org/licenses/by/4.0/), which permits use, distribution and reproduction in any medium, provided the original work is properly cited.

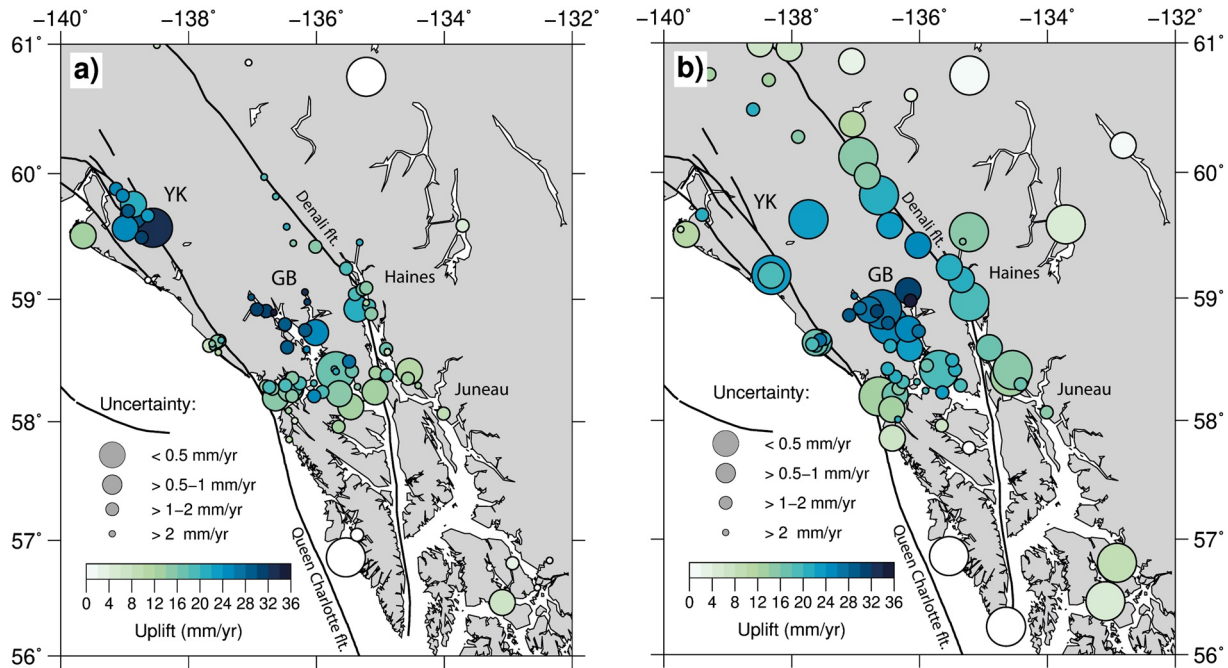


Figure 1. Average GPS uplift rates (mm/yr) over the periods (a) 1992–2003 and (b) 2003–2012 derived by Hu and Freymueller (2019). Two uplift peaks with rates >30 mm/yr can be seen at the Yakutat and Glacier Bay ice fields. Mapped quaternary faults are obtained from the Alaska Quaternary fault and folds database (Koehler, 2013).

the eighteenth century in the GB area, and at the end of the nineteenth century near the YK ice field (Larsen et al., 2005).

To model the Earth's viscoelastic response to changes in ice loading, previous GIA studies (e.g., Elliott et al., 2010; Hu & Freymueller, 2019; Larsen et al., 2005; Sato et al., 2011) have made use of GPS uplift rates to optimize three key parameters in a 1-D Earth model: the effective elastic lithospheric thickness, the asthenospheric viscosity, and its thickness. Larsen et al. (2005) made use of the TABOO software by Spada (2003) and Spada et al. (2003) based on the stratified, non-rotating, self-gravitating, spherical, incompressible Maxwell Earth developed by Sabadini et al. (1982). They found that a thin elastic lithosphere (60–70 km) combined with a low-viscosity asthenosphere ($2.5\text{--}4.0 \times 10^{18}$ Pa-s) were required to fit the observations. Subsequent studies (Elliott et al., 2010; Hu & Freymueller, 2019; Larsen et al., 2005) added new GPS data, increased the spatial resolution of the GIA model and updated the ice load model to account for the increasing PDIM. An overview of their optimal Earth model parameters is seen in Table 1. The maximum spherical harmonic components (degree and order) in Larsen et al. (2005) are 1,024, whereas

Table 1
Earth Model Parameters From Various Glacial Isostatic Adjustment Studies in Southeastern Alaska

Study	Lithospheric thickness (km)	Asthenospheric thickness (km)	Asthenospheric viscosity (Pa-s)	Upper mantle viscosity (Pa-s)	Largest update
Larsen et al. (2005)	60–70	110	$2.5\text{--}4.0 \times 10^{18}$	4.0×10^{20}	–
Elliott et al. (2010)	50	110	3.7×10^{19}	4.0×10^{20}	GPS
Sato et al. (2011) (two-layer mantle)	54	110	5.6×10^{19}	4.0×10^{20}	GPS + ice model
Sato et al. (2011) (four-layer mantle)	60	160	1×10^{19}	^a	GPS + ice model
Hu and Freymueller (2019)	55	230	3×10^{19}	^b	GPS + ice model

^aFour-layer model: viscosities 3, 3, and 4 in units of 10^{20} Pa-s for the upper and lower parts of the upper mantle, and the lower mantle, respectively. ^bUpper part and lower parts have viscosities of 2.4×10^{21} and 5×10^{21} Pa-s, respectively. Hu and Freymueller (2019) adopt the VM5a model (Argus & Peltier, 2010; Peltier, 2004; Peltier et al., 2015) for deeper viscosities.

Elliott et al. (2010) and subsequent studies increased the spherical harmonics up to degree and order 2,048. This way, small ice load changes and their effects could be resolved with higher spatial detail. In addition, Elliott et al. (2010) used a refined GPS data set with higher accuracy and density. This mainly resulted in constraints with a thinner lithosphere. Sato et al. (2011) investigated increased PDIM rates using the ice-rate model by Larsen et al. (2007), which resulted in a larger asthenospheric thickness being required to fit the data. Hu and Freymueller (2019) modeled higher PDIM rates, derived from the ice-rate model from Berthier et al. (2010). Overall, a thin lithosphere (50–70 km) underlain with a low-viscosity asthenosphere (2.5×10^{18} – 3×10^{19} Pa-s) is preferred. However, some areas remain either underpredicted (e.g., the YK ice fields) or overpredicted (e.g., Haines to Juneau) (Hu & Freymueller, 2019). These discrepancies are likely due to systematic errors in the ice load model or the Earth model.

The 1-D parameterization in previous GIA studies may not accurately represent the true 3-D Earth structure in this region which may affect the GIA predictions. Studies of other regions have shown that a 3-D structure has a large impact on the GIA predictions (e.g., Li et al., 2020; Spada et al., 2006; van der Wal et al., 2013). Global seismic tomography studies (e.g., Schaeffer & Lebedev, 2013) and a regional tomography study for Alaska by Jiang et al. (2018) show that lateral variations in seismic velocities exist in the region, which likely correspond to variations in temperature and composition. The actual 3-D structure in Southeast Alaska is more complex due to the geologic history of tectonism. Before 40–60 million years ago, depending on the plate reconstruction considered, this region was a subduction zone (Engelbreton et al., 1984; Fuston & Wu, 2020; Haeussler et al., 2003). Since that time, the region has been subjected to shear deformation and substantial margin-parallel (northward) transport of material via strike-slip faulting (DeMets & Merkouriev, 2016). Offshore of Southeast Alaska, there is an abrupt transition from continental to oceanic lithosphere across the Queen Charlotte fault.

Seismic anomalies can be converted to viscosity variations. For example, Ivins and Sammis (1995) used a scaling relationship for the conversion, by relating density anomalies to temperature anomalies based on the notion that seismic anomalies are caused by temperature variations alone. In reality, non-thermal effects such as compositional heterogeneity can also affect seismic anomalies. Non-thermal effects can also play a role in continental regions characterized by iron depletion or in tectonically active regions (i.e., characterized by partial melt and/or high water content) (Artemieva et al., 2004). In the GIA studies by Wang et al. (2008) and Wu et al. (2013), the scaling relationship of Ivins and Sammis (1995) is multiplied by a scaling factor, which represents the fractional thermal contribution to seismic anomalies. Wu et al. (2013) found a best fit to GIA observations for the case that thermal effects have a dominant control over seismic anomalies beneath Fennoscandia, with 65% control in the upper mantle which increases with depth into the lower mantle. However, uncertainties related to the relative thermal contributions increase with depth because the GIA process in Scandinavia is mostly sensitive to the upper mantle. Other methods to determine viscosity rely on flow laws and an estimate of mantle temperature (e.g., van der Wal et al., 2013).

In this work, we will mainly use the method of Wu et al. (2013) to constrain the thermal effect on seismic anomalies by using seismic tomography and GIA due to post-LIA ice load changes. Because of the short wavelength of the ice load, we restrict the investigation to parameters in the shallow upper mantle (<400 km), since crustal velocities are not very sensitive to viscoelastic relaxation in deeper mantle layers (Hu & Freymueller, 2019). A secondary aim of this research is to determine the importance of 3-D viscosity structure for this regional loading problem, considering the high computational cost of 3-D models. The scaling factor, which represents the fractional thermal contribution, is also a measure for the magnitude of viscosity variations. Therefore, the obtained scaling value will reveal to what extent 3-D viscosities play a role in the area. Predictions for 3-D models are compared to those of 1-D models.

To summarize, we aim to answer the following research questions:

1. How do GIA models constrain the regional 3-D viscosity structure?
2. What is the thermal contribution to shear wave anomalies in the region?
3. What is the effect of lateral viscosity variations on GIA model predictions?

The GIA modeling was performed with a Finite Element (FE) model which allows lateral heterogeneity. Section 2.1 of this paper explains the FE model setup and the Earth model parameters. Section 2.2 briefly describes the ice load model and Section 2.3 describes the method to retrieve viscosities from seismic

tomography. The suite of viscosity models explored in this area are presented in Section 3.1. In Section 3.2, the model misfits are evaluated using a chi-square test. The role of 3-D viscosity variations is evaluated in Section 3.3. An alternative approach to retrieving a 3-D viscosity distribution is throughflow laws for olivine, where 3-D variations result from variations in temperature. We evaluate this approach in Section 3.4. To compare our results with earlier studies, which are all based on incompressible earth models, we address the role of material compressibility in Section 3.5. Implications of our results for the regional Earth structure are discussed in Section 3.6. Model limitations are described in Section 3.7, followed by the conclusions.

2. Methods

2.1. Model Setup and Geometry

In this research, the FE method is used to model deformation and stress in the Earth as implemented in the commercial FE package ABAQUS FEA (Hibbitt et al., 2016), following the approach by Wu (2004). The GIA model in this research adopts a flat-Earth approximation. The validity of the flat-Earth approximation was shown in Wu and Johnston (1998) for loads up to the size of the Fennoscandian ice sheet. Hence, the flat-Earth assumption is reasonable considering the smaller extent of the ice load in Alaska since the LIA. In addition, material compressibility is assumed, while the density perturbations associated with volumetric deformation are neglected. Compressibility effects on the buoyancy force are expected to mainly affect the horizontal displacement (Tanaka et al., 2011) which is not considered in this study. Moreover, self-gravitation is neglected. Amelung and Wolf (1994) showed that the effect of neglecting self-gravitation is partly counteracted by the flat-Earth approximation, which was also confirmed in Spada et al. (2011) and Schotman et al. (2008).

The incompressible flat-Earth FE model has been benchmarked against the normal-mode (NM) model of Hu and Freymueller (2019) (see Supporting Information S1). The FE and NM models show good agreement, where most of the difference are smaller than 1 mm/yr. The largest differences (up to 2.5 mm/yr) are near the YK ice fields, which are likely due to smoothing of the ice load model in the FE grid and approximation in the FE models. In addition, tests were performed on the FE model resolution with 10 and 15 km. The NM model uses spherical harmonics with maximum order and degree of 2,048 (~10 km). The 10 km FE resolution model did not yield significantly better results than the 15 km resolution test (differences less than 0.5 mm/yr) and resulted in much longer computational times. For that reason, the 15 km resolution was used in further simulations as it was adequate to represent the observed deformation. For further details on the model the reader is referred to the Supporting Information S1.

The model geometry is based on work by Schotman et al. (2009) and Barnhoorn et al. (2011). The loading area consists of 155×95 elements with the above-mentioned resolution of 15×15 km. Deeper layers (starting from 90 km) have a coarser resolution: 31×19 elements of 75×75 km. Figure 2 shows the model surface geometry. The total surface area of the model is $20,000 \times 20,000$ km and the model extends to a depth of 10,000 km in order to minimize boundary effects. In total, 26 FE layers are created, which gives a total of 198,530 elements. The bottom and vertical edges are prescribed with boundary conditions such that the bottom edge is fixed, and the sides are limited to vertical translation. Winkler foundations (Wu, 2004) are applied at the Earth's surface and internal boundaries where density jumps occur to simulate buoyancy forces.

The shallower layers of the model have a higher resolution, whereas the deeper layers have lower resolution. The resolution of these two parts is chosen such that an even number of elements of the higher resolution part fit exactly on the top surface of the lower resolution part. Considering the mismatch in nodes and the fact that ABAQUS does not provide a standard element to model this, tie constraints are applied at the two surfaces where resolution jumps occur. The tie constraints allow for all active degrees of freedom to be equal for both surfaces. The two surfaces are defined by the upper and lower element surfaces of the two layers, respectively. The outer vertical edge elements are not taken into account as these element nodes already have a fixed constraint.

The Earth model parameters are described in Table 2. The density and shear modulus are derived from volume-averaging the PREM model (Dziewonski & Anderson, 1981). The Young's modulus (E) is required as input by ABAQUS and is computed using $E = 2G(1 + \nu)$, where G is the rigidity and ν is Poisson's ratio. Durkin et al. (2019) used the LITHO1.0 lithosphere model (Pasyanos et al., 2014) to infer variations in the

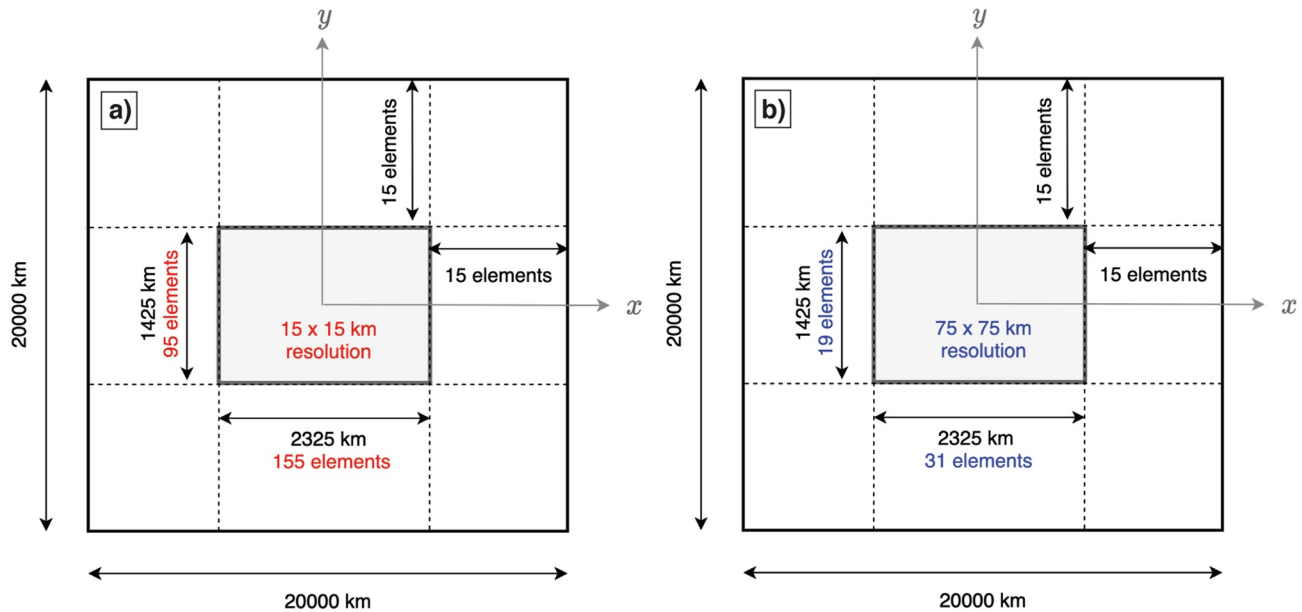


Figure 2. Horizontal geometry. The upper six layers have a higher horizontal resolution of 15 km (a), whereas the lower layers have a lower horizontal resolution of 75 km (b).

density and elastic structure and showed that lateral variations in these parameters have a small effect on the elastic uplift. We therefore do not include a laterally heterogeneous density and elastic structure. Poisson's ratio varies with depth between 0.26 and 0.30.

The upper three layers (depth <40 km) are considered fully elastic. Below 400 km depth, the viscosity is only varying with depth. Sato et al. (2011) showed that GIA is less sensitive to viscosity values below this depth due to the short wavelength of the ice load involved. Therefore, we consider it reasonable to use viscosities from a global reference model below 400 km depth and the VM5a model (Peltier et al., 2015) was adopted for this purpose. Below 40 km and above 400 km depth, each individual element within a layer is assigned to an individual viscosity value.

2.2. Ice Load Model

Upon ice removal, the Earth responds with an instantaneous elastic response and a time-delayed viscous response. The timescale associated with the viscous flow is related to the characteristic relaxation time of the mantle. Due to the presence of low viscosities in the asthenosphere, the associated relaxation times are decades to years, which are comparable to the timescales of recent ice loss and make it difficult to separate elastic and viscous processes. For that reason, both LIA and PDIM glacier variations are modeled together in the ice model.

The ice load model is adopted from Hu and Freymueller (2019). We shortly summarize its main characteristics here, but the reader is referred to Hu and Freymueller (2019) for further details. The ice load model is assumed to be a function of space and time, where the ice evolution spans the last 2 ka. In essence, the ice load model consists of three sub-models defined for selected areas: the whole region, GB and the YK ice fields. The last two are necessary because ice mass loss was asynchronous with respect to the regional model. The GB ice field experienced a large ice volume loss about 200 years ago and the YK ice field experienced an accelerated ice mass loss during the last two decades. The reader is referred to Figure 5b in Hu and Freymueller (2019) for the time history of the ice loads. The glacier evolution is essentially the same as in Larsen et al. (2005), except for the adoption of the late twentieth century ice rate map from Berthier et al. (2010) (here referred to as the Berthier model). The data used for the Berthier model covers the period between 1962 and 2006. In their ice model, Hu and Freymueller (2019) assume these rates to represent the average ice wastages between 1900 and 1,995. For PDIM rates (1,995–2,012) the Berthier model is extrapolated and

Table 2
Model Layers and Earth Parameters

Top of layer radius (km)	Layer thickness (km)	Density (kg/m ³)	Rigidity (GPa)	Youngs modulus (GPa)	Poisson's ratio	Viscosity (Pa-s)
6,371	12	2,171.5	26.6	68.1	0.28	–
6,359	14	2,885.1	42.8	109.6	0.28	–
6,345	14	3,380.3	68.1	174.4	0.28	–
6,331	15	3,378.0	67.9	174.2	0.28	T.B.D.
6,316	15	3,376.6	67.7	173.5	0.28	T.B.D.
6,301	20	3,375.2	67.5	172.9	0.28	T.B.D.
6,281	20	3,372.5	67.1	171.8	0.28	T.B.D.
6,261	20	3,370.9	66.9	171.0	0.28	T.B.D.
6,241	20	3,369.2	66.7	170.1	0.27	T.B.D.
6,221	20	3,365.8	66.3	168.8	0.27	T.B.D.
6,201	20	3,372.9	67.1	170.4	0.27	T.B.D.
6,181	20	3,380.0	67.9	172.0	0.27	T.B.D.
6,161	20	3,416.2	71.5	180.8	0.26	T.B.D.
6,141	20	3,452.4	75.1	189.5	0.26	T.B.D.
6,121	40	3,463.7	75.8	190.7	0.26	T.B.D.
6,081	50	3,486.1	77.1	199.3	0.29	T.B.D.
6,031	60	3,706.4	92.4	239.5	0.30	T.B.D.
5,971	135	3,781.5	116.4	302.3	0.30	5.0×10^{20}
5,836	135	3,950.7	117.9	304.6	0.29	5.0×10^{20}
5,701	250	4,443.9	170.1	439.2	0.29	1.6×10^{21}
5,451	250	4,590.3	188.5	479.4	0.27	1.6×10^{21}
5,201	430	4,780.0	208.8	533.8	0.28	3.2×10^{21}
4,771	430	5,008.7	233.7	601.6	0.29	3.2×10^{21}
4,341	430	5,227.8	258.4	668.5	0.29	3.2×10^{21}
3,911	431	5,444.1	283.4	736.6	0.30	3.2×10^{21}
3,480	3,480	10,925.0	–	–	–	–

Note. Density and Young's modulus are derived from volume-averaged PREM values. Viscosity below 400 km depth follows the VM5a viscosity model. The viscosity between 40 and 400 km depth are determined through scaling the seismic model. T.B.D. = to be determined.

ice wastage is enhanced by a factor of 1.8 and 2.2 for the periods 1995–2003 and 2,003–2,012, respectively. PDIM has a contribution to the current uplift rates of up to 45% and 25% for YK and GB, respectively (see Figure S7 in Supporting Information S1), which is larger than the values found in Larsen et al. (2005). This is largely attributed to the higher PDIM rates modeled.

The regional ice load model is given by 677 disks with radii between 10 and 11 km, whereas the GB ice load model is represented by 5 additional disks with radii between 13 and 19.5 km. The disks around YK, which are given by the regional model, are subjected to ice loss rates three times larger than the regional model. This loading is interpolated to the FE grid, while conserving total mass change at each time step. The fraction of each disk covered by a rectangular FE grid element is assigned to a rectangular grid cell. The ice load distribution is shown in Figure S3 in Supporting Information S1. The mesh size needs to be small enough so that errors around the ice load edges are minimized. Our benchmark analysis (see Supporting Information S1) showed that a resolution of 15 km was sufficient to this end.

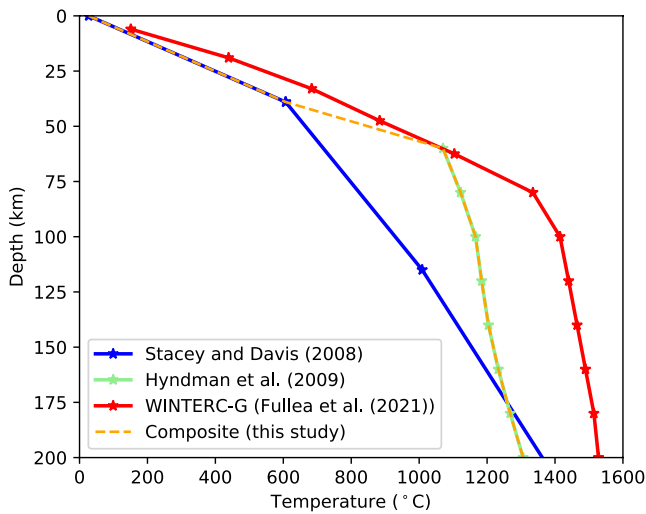


Figure 3. Averaged temperature profiles by selected studies. Hyndman et al. (2009) focus on the Northern Cordillera, whereas WINTERC-G (Fullea et al., 2021) represents a global 3-D temperature and Stacey and Davis (2008) represent global 1-D temperatures. The WINTERC-G temperature are averaged within the area bounded by latitudes 58°–60°N, and longitudes 135°–141°W.

2.3. 3-D Viscosity Calculations From Seismic Velocity Anomalies

The 3-D viscosity structure is estimated directly through seismic tomography as described in the approach by Wu et al. (2013). In the crust seismic anomalies are mainly controlled by composition, whereas in the upper mantle seismic wave anomalies are for a large portion controlled by temperature (e.g., Cammarano et al., 2003; Goes et al., 2000; Hyndman, 2017). Assuming that temperature variations are responsible for viscosity anomalies, Ivins and Sammis (1995) introduced a scaling relationship between seismic velocity anomaly and viscosity that computes viscosity anomalies based on the effect of temperature and mineral physics. Wu et al. (2013) slightly modified this relationship and included a parameter to scale the viscosity anomaly based on the thermal contribution. The scaling relationship is given by (Wu et al., 2013):

$$\log_{10}(\Delta \eta) = \frac{-\log_{10}(e)\beta}{\left[\frac{\partial \ln v_s}{\partial T}\right]_{\text{tot}}} \frac{E + PV}{RT_0^2} \frac{\partial v_s}{v_{s,0}}, \quad (1)$$

where β is a scaling factor ($\beta \in [0,1]$) representing the thermal contribution to shear wave anomalies, e is Euler's number, T_0 is the background temperature as a function of depth (assumed to be 1-D), E is the activation energy, P is the pressure, V is the activation volume, R is the gas constant,

$\frac{\partial v_s}{v_{s,0}}$ is the fractional shear wave anomaly computed with respect to

the reference seismic anomaly profile $v_{s,0}$, and $\left[\frac{\partial \ln v_s}{\partial T}\right]_{\text{tot}}$ is the velocity derivative with respect to temperature accounting for both anharmonic and anelastic effects. Thus 3-D temperature variations are determined from the seismic velocity variations (scaled by the parameter β), and viscosity variations are inferred from the temperature variations. The absolute viscosity is then related to the background viscosity and the viscosity anomalies with $\Delta \eta \equiv \eta / \eta_0$.

The seismic anomalies are taken from the global shear wave velocity model SL2013sv (Schaeffer & Lebedev, 2013). This model defines lateral variations in velocity with respect to a 1-D velocity profile for the mantle (<1,000 km). Although uncertainties associated with the input velocity model can influence the results (e.g., Yousefi et al., 2021), we do not consider them. Shear wave velocity anomalies in Southeast Alaska are dominantly negative (see Figure 4, upper panels), which result in lower viscosities and thus a weakening effect on the upper mantle rheology. The velocity derivatives in Equation 1 are taken from Table 20.2 in Karato (2008), which represent global averages and may introduce a bias for Southeast Alaska; anelasticity is expected to play a larger role in this area due to the higher temperatures involved (Hyndman et al., 2009). Also, if indeed the mantle is substantially hydrated, the increased water content will enhance the anelasticity effects (Hyndman et al., 2009). If anelastic effects are not taken into account (or not enough), temperatures could be overestimated and in turn result in lower viscosities. Uncertainties related to the effect of the composition, water content and partial melt, are not considered here and may also affect the β parameter.

The 1-D background temperature profile (T_0) used in Equation 1 is a composite of the globally averaged profile by Stacey and Davis (2008) and the regional study by Hyndman et al. (2009). Temperatures between 0 and 39 km depth are taken from Stacey and Davis (2008) and between 60 and 200 km from Hyndman et al. (2009) (model C8 in their appendix), while they are linearly interpolated between 39 and 60 km. Temperatures below 200 km the temperature follows the adiabatic gradient of 0.4 K/km, as shown in Figure 3. A globally averaged profile, such as the Stacey and Davis (2008) temperature profile results in a too thick elastic lithosphere, whereas previous GIA studies have shown that a thin elastic lid (50–70 km) is required to fit the crustal deformations (Hu & Freymueller, 2019; Larsen et al., 2005; Sato et al., 2011). Therefore, the globally averaged profile is not considered suitable.

The search space consists of the background viscosity profile and the β parameter in the upper mantle. We limit the search grid to the upper mantle as GIA does not constrain deeper viscosities due to the short

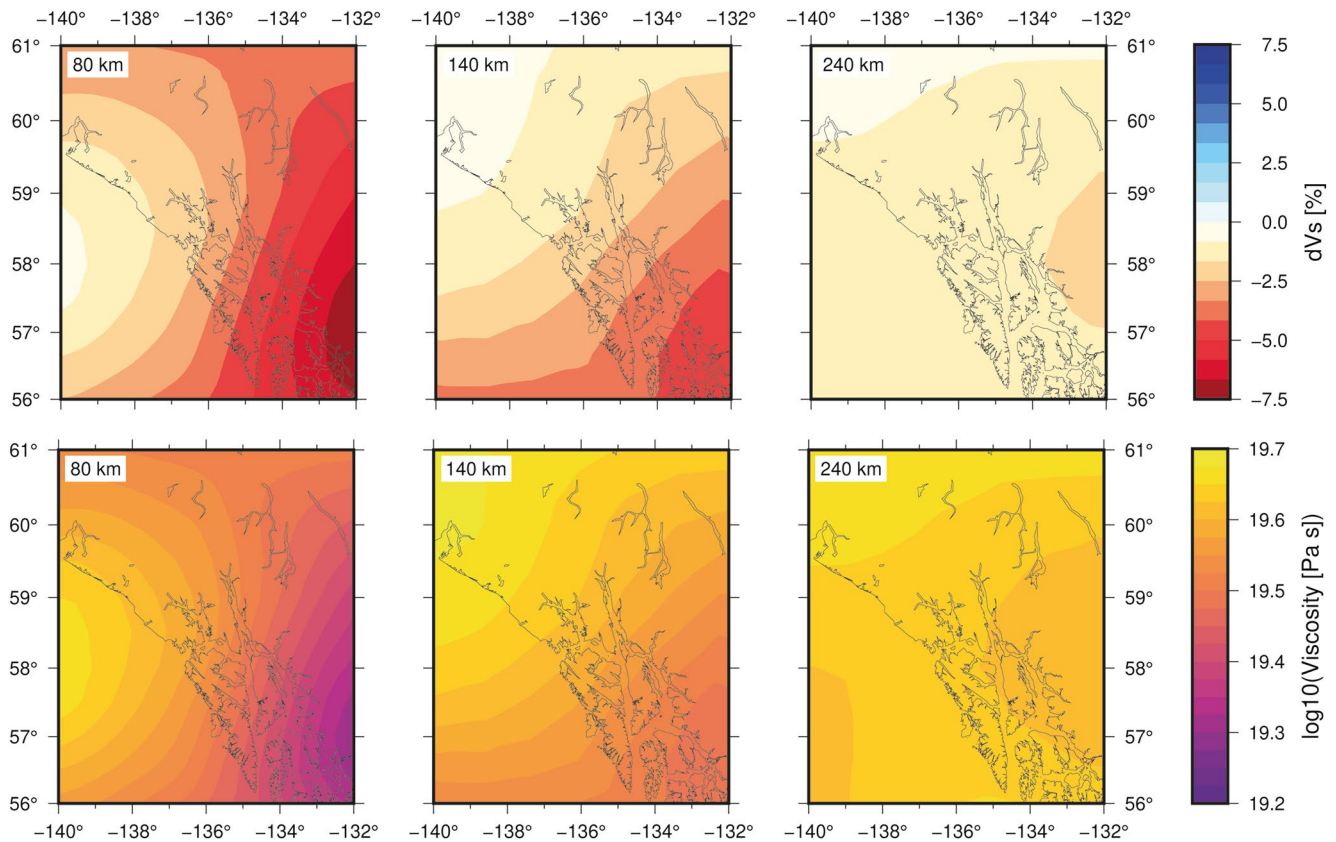


Figure 4. Shear wave anomaly and viscosity maps at depths 80, 140, and 240 km. Shear wave anomalies were linearly interpolated from the SL2013sv model (Schaeffer & Lebedev, 2013). Negative shear wave anomalies indicate larger temperatures and thus lower viscosities. The largest contrasts are at a depth of 80 km and lateral variations reduce with depth.

wavelength of the regional deglaciation (e.g., Hu & Freymueller, 2019; Larsen et al., 2005; Sato et al., 2011). Choosing the background viscosity should be done carefully. The VM5a viscosity structure is not suitable for this area due to its relatively high viscosity in the upper mantle: 10.0×10^{21} (between 60 and 100 km) and 0.5×10^{21} (between 100 and 420 km) Pa-s, as opposed to the range (2.5×10^{18} – 3.0×10^{19} Pa-s) for the asthenosphere found in regional GIA studies (e.g., Hu & Freymueller, 2019; Larsen et al., 2005; Sato et al., 2011). We selected the best-fit earth model of Hu and Freymueller (2019) as the baseline for comparison with our analysis: the elastic lithosphere is 55-km thick and the asthenosphere is 230-km thick with a viscosity of 3.0×10^{19} Pa-s.

3. Results and Discussion

3.1. Viscosity Variations and 1-D Averaged Profiles

The mantle viscosity throughout the volume was computed following Equation 1. Lateral viscosities at selected depths for the best fit model (described in Sections 3.2 and 3.3) are depicted in Figure 4 (lower panels). The seismic anomalies are directly related to the viscosities; negative shear wave anomalies indicate larger temperatures and thus lower viscosities. The largest variations are seen at approximately 80 km and variations decrease with depth. In deeper layers, the viscosity variations decrease as seismic velocity variations decrease, because we use a constant scaling relation throughout the mantle. In addition, we ran a number of models using an alternative approach (described in Section 3.4), which entails inferring viscosities from temperature variations from the global temperature model WINTERC-G (Fullea et al., 2021) throughflow laws for olivine (Hirth & Kohlstedt, 2003).

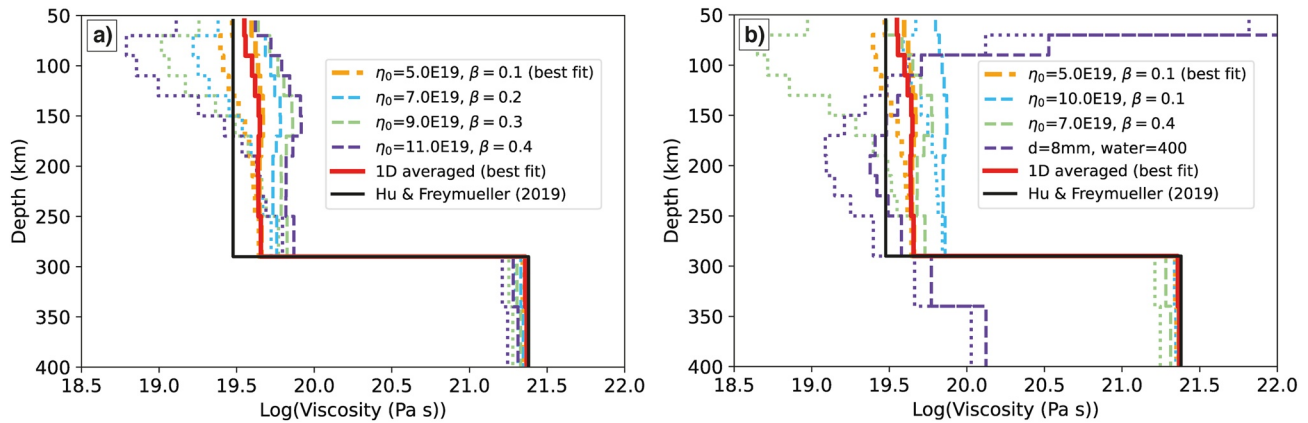


Figure 5. Viscosity profiles derived from shear wave velocity anomalies for selected background viscosity (η_0) and scaling factor (β). The viscosity profiles are taken at two points; 133.6°W, 57.3°N (dotted) and 138.8°W, 59.3°N (dashed) representing the minimum and maximum profiles of the 3-D structure. The profiles in panel (a) represent the combinations along the diagonal in Figure 6a with relatively low χ^2 values, which have similar average viscosities. The profiles in panel (b) result in large χ^2 values (except for the orange, red and black lines). The orange lines show the viscosity profiles of the 3-D best fit model and the red lines show the averaged 1-D viscosity of the model. The purple lines in plot b represent the best fit 3-D model obtained throughflow laws for olivine by varying the grain size and water content. The black line was the result of the best fit 1-D incompressible model in Hu and Freymueller (2019).

Upper and lower bounds on the 3-D viscosity variations with depth are shown in Figure 5a for several combinations of the adjustable parameters η_0 and β . These profiles illustrate a tradeoff between these two parameter values for models providing a good fit to the GPS observations, such that the scaling factor β needs to be larger for models with a higher background viscosity in order to fit the data well. All of these models have relatively similar 1-D average viscosity profiles, with the lowest viscosities always located at shallow depth in the southeastern part of the model domain (Figure 4, left panels). However, a lower background viscosity combined with small lateral viscosity variations results in the best fit. The acceptable combinations for η_0 and β are seen in Figure 6a, which are an approximation of a 2σ uncertainty based on a 20% misfit increase.

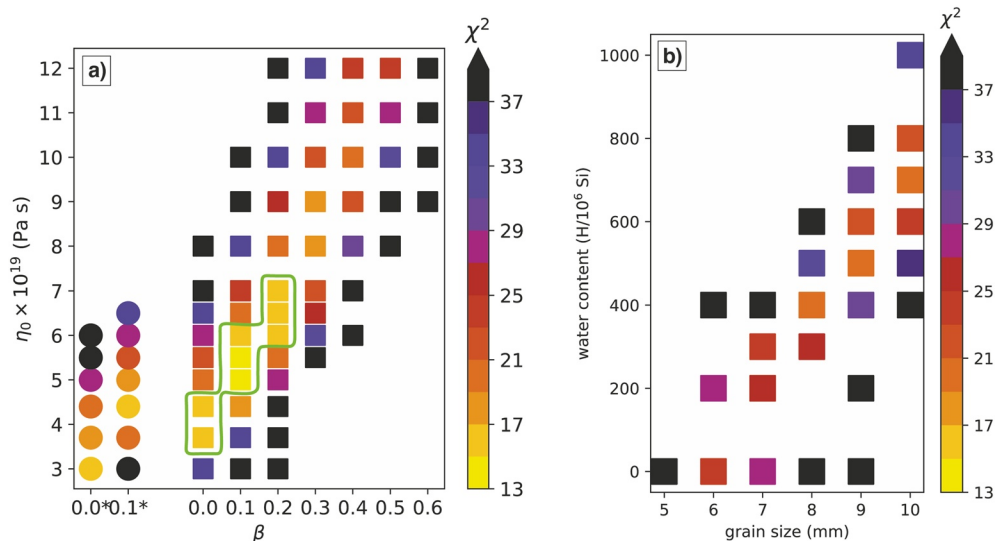


Figure 6. (a) Scatter plot of χ^2 values where the viscosity distribution is obtained directly from shear wave velocity anomalies. (b) Scatter plot of χ^2 values obtained by using flow laws for olivine. The models are compressible with some exceptions made in panel (b) where round symbols indicate results from incompressible models. The best fit model ($\chi^2 = 13.7$) is obtained for the scaled seismic anomalies approach with scaling factor 0.1 and background viscosity 5.0×10^{19} Pa-s. The green outline in panel (a) corresponds to models with an increase in $\chi^2 < 20\%$ with respect to the best fit model, which is an approximation of a 2σ uncertainty.

For the profiles shown in Figure 5b, the averaged viscosity is either too low or too high, resulting in poor prediction of the uplift rates. For example, the green line in Figure 5b has, on average, a lower viscosity than the best fit model, and the blue line has higher averaged viscosities. All of the viscosity models based on the WINTERC-G temperature model performed poorly (Section 3.4). The best-fit profile from this approach is indicated in Figure 5b (purple lines). This approach did not yield good fits because the thick lithosphere imposed by the global temperature model WINTERC-G is incompatible with the thin lithosphere required in this region (Figure 3). Further details on the results of this approach are discussed in Section 3.4.

3.2. Model Performance

The GIA model performance is tested against the GPS rates from Hu and Freymueller (2019), shown in Figure 1. The vertical uplift is due to the combined effect of GIA due to post-LIA, PDIM, and Pleistocene glaciations. In this study, we only modeled post-LIA and PDIM effects. We superimpose our modeled results with the effects of Pleistocene glaciations modeled in Hu and Freymueller (2019). The impacts of Pleistocene glaciations include contributions of the Laurentide ice sheet (ICE-3G), glaciers in southern Alaska (Wheeler, 2013) and glaciations of southern British Columbia and Cascadia (James et al., 2009), and are very small in this region (on the order of 1 mm/yr). These Pleistocene glaciations effects were computed by Hu and Freymueller (2019) using a NM GIA model, which may not represent the effects with a FE model with different Earth parameters. However, the effects by Pleistocene glaciations are sufficiently small that the overall difference is assumed to be negligible. We do not consider tectonic effects as these effects are expected to be small because of the largely strike-slip tectonics (Elliott et al., 2010) (e.g., <2 mm/yr for the fault system in southern California (Smith-Konter et al., 2014)). The misfits between the observed and predicted GIA rates are evaluated using the χ^2 test:

$$\chi^2 = \frac{1}{N} \sum_{i=1}^N \left(\frac{o_i - p_i}{\sigma_i} \right)^2, \quad (2)$$

where N is the number of observations, o_i is the observed GPS rate, p_i is the predicted uplift rate (including Pleistocene glaciations, LIA, and PDIM effects) and σ_i the GPS error. GPS observations are available for two periods: 1992–2003 and 2003–2012. Observations of both periods are combined to compute the best-fit value. Note that we do not include the error in the Pleistocene glaciation, LIA and PDIM loading models as there is no good error information available for these models.

The viscosities of the best fit model vary between 1.8×10^{19} and 4.5×10^{19} Pa-s. Viscosity maps at selected depths are shown in Figure 4 (lower panels). The 3-D viscosities of the best fit model are in the same range as found in previous 1-D GIA modeling studies (e.g., Hu & Freymueller, 2019; Larsen et al., 2005; Sato et al., 2011). However, a large portion of the 3-D viscosities is larger than the previous 1-D GIA model, which is attributed to the inclusion of compressibility in our model (see Section 3.5). Figure 6a shows that incompressible models prefer a lower background viscosity than compressible models with the same scaling parameter. Present-day velocities increase for a compressible model in comparison to an incompressible model with the same earth model parameters. Thus, an incompressible model would require lower viscosities to achieve similar uplift rates as compressible model, given the loading model. Tanaka et al. (2011) showed that incompressible models underestimate the viscosity, which agrees with our results. Next, we investigate if the lateral variations for our best fit model are significant enough to be differentiated from a 1-D model with the GPS uplift rate data.

3.3. Role of 3-D Viscosities in the Upper Mantle

The optimal background viscosity and the scaling parameter are $\eta_0 = 5.0 \times 10^{19}$ Pa-s and $\beta = 0.1$ (Figure 6a), respectively. The best-fit model has a fit value of $\chi^2 = 13.7$ with residual mean of 0.3 ± 3.92 mm/yr. The residuals of the 3-D model are shown in Figures 7a and 7d. This 3-D model was able to reduce the residuals with respect to the best-fit 1-D model in Hu and Freymueller (2019); most reductions are located inland and along the Lynn Canal, the inlet from Haines to Juneau. Because the 1-D model in Hu and Freymueller (2019) is incompressible, we compare the 3-D model with a “1-D averaged” model, where the viscosity structure is derived from the best fit 3-D model by averaging the viscosity in each layer over a certain area.

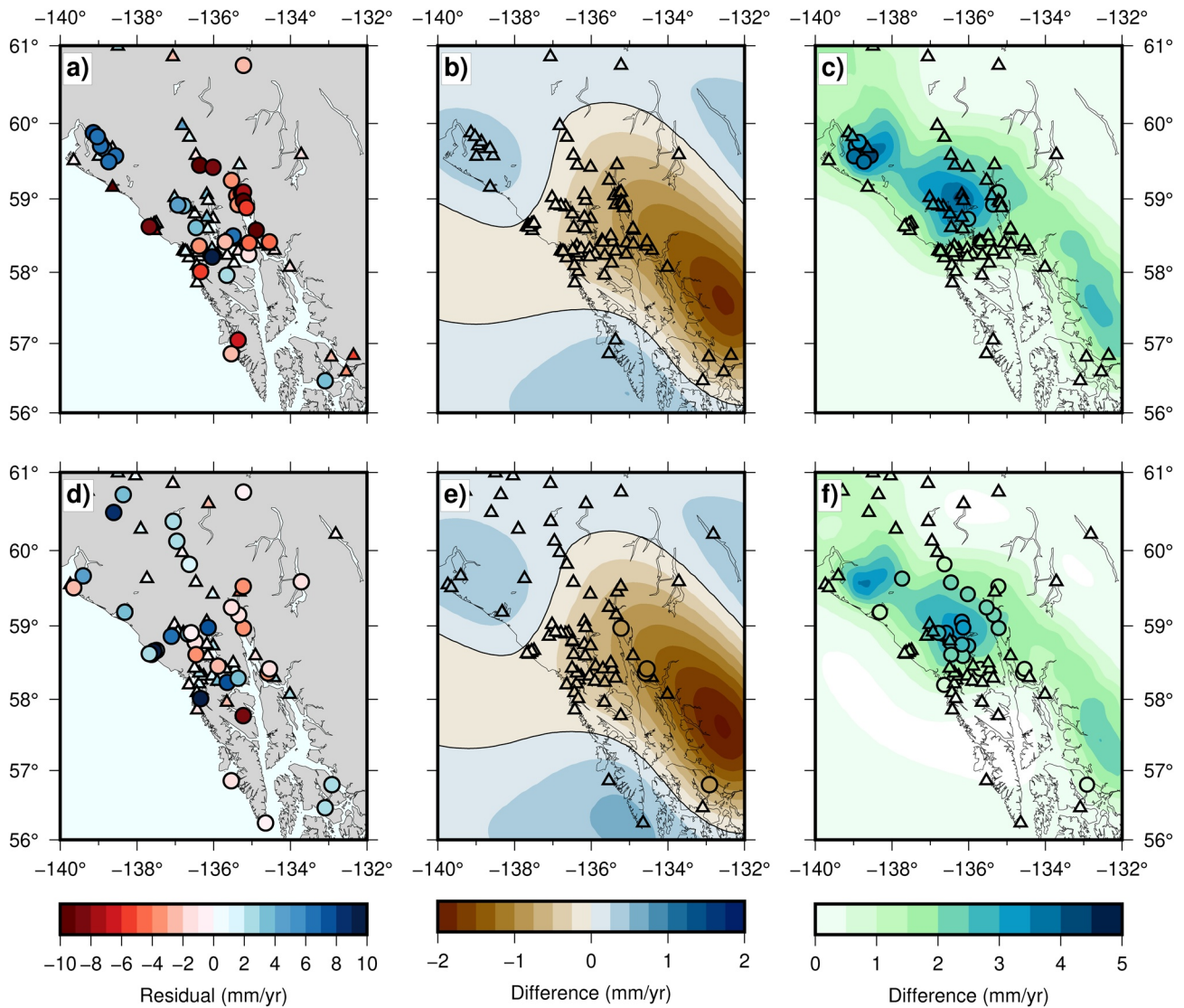


Figure 7. (a) Residuals of the uplift predictions between 1992 and 2003 of the best fit 3-D model; (b) differences in uplift (1992–2003) between the best fit 3-D model and averaged 1-D model; (c) difference in uplift (1992–2003) between the best fit 3-D compressible model and 3-D incompressible model; (d) residuals of the uplift predictions between 2003 and 2012 of the best fit 3-D model; (e) differences in uplift (2003–2012) between the best fit 3-D and averaged 1-D model; and (f) difference in uplift (2003–2012) between the best fit 3-D compressible model and 3-D incompressible model. Triangles indicate that the models cannot be differentiated within 2σ uncertainty, whereas circles show that they can be resolved. Negative (positive) values in panels (b) and (e) indicate larger (smaller) uplift predictions for the 3-D model. An incompressible model results in smaller uplift predictions than a compressible model, therefore, panels (c) and (f) only show positive values.

The area is confined to grid cells with prediction rates larger than 15 mm/yr. The viscosity profile can be seen in Figure 5a, which shows that the 1-D viscosity profile is closer to the upper bound of the viscosity variations in the 3-D structure. The 1-D averaged model has a fit value of $\chi^2 = 12.1$. We also tested thresholds of 5, 10 and 20 mm/yr, which resulted in a change of +0.2, +0.3, and 0.0 in the χ^2 value, respectively. Thus, we conclude that the averaging is not very sensitive to the considered test areas.

The differences between the 3-D and 1-D averaged model uplift prediction rates are shown in Figures 7b and 7e. The largest differences in the uplift occur in the southeastern corner (up to -2 mm/yr), which is where the largest variations in seismic velocity and thus viscosity are located. However, there are few observations available where the largest differences occur. We do see that the 1-D model systematically performs better than the 3-D model along Lynn Canal, the inlet from Haines to Juneau (Figure S5 in Supporting Information S1). For the 3-D case, this corresponds to the zone where seismic velocity anomalies were most

negative (where there are GPS measurements) and hence the viscosity becomes lower than its surroundings at shallow depths (Figure 4). This results in too large uplift rates for the 3-D model, while the 1-D model predictions are smaller and closer to the observations. The 3-D model systematically performs better around GB; however, the difference is within the GPS uncertainties. It is possible that, errors in the seismic velocity model make the 3-D model fit slightly worse than the 1-D model, or the contribution of temperature variation to viscosity might not be uniform over the area. Overall, most of the differences are smaller than 2σ , indicating that the 3-D and 1-D models cannot be differentiated from each other (Figures 7b and 7e). This implies that lateral variations do not impact the predicted uplift rate significantly.

3.4. Comparisons to 3-D Viscosities Derived From Olivine Flow Laws

An alternative approach to determine the 3-D viscosity variations is by using flow laws for creep of olivine. Here, we use the same methods in van der Wal et al. (2013) for diffusion creep. For this approach, viscosities are inferred from lateral variations in temperature, water content and grain size are varied and a best fit with the GPS data is sought. We use the global temperature model WINTERC-G by Fulla et al. (2021), for which the average temperature profile beneath Southeast Alaska is shown in Figure 3. Water content and grain size shift the viscosity profile (the purple line in Figure 5b), whereas the temperature model determines the shape of the profile and the magnitude of the viscosity variations. For details on the method and considered parameter values, the reader is referred to the Supporting Information S1. Note that the WINTERC-G provides absolute temperatures; it is therefore not possible to use composite background temperatures shown in Figure 3 for the 3-D temperature field. We could have opted to use the 3-D temperatures derived from the background geotherm and seismic anomalies, but such a model would not be independent. Furthermore, the results show that the lithosphere of the 3-D models is likely too thick. Since WINTERC-G already has the largest temperatures (Figure 3); replacing WINTERC-G based temperatures with the seismically derived temperatures would exacerbate this problem.

The fit results (χ^2) are seen in Figure 6b. The plot shows that similar fits can be obtained with certain combinations of water content and grain size: if we increase the water content (a weakening effect), then we need to increase the grain size (a strengthening effect). The best fit parameters of 8 mm grain size and 400 ppm H₂O result in a fit value of $\chi^2 = 20.1$. The best fit value of 20.1 is, however, more than 50% larger than the values obtained with the scaling of shear wave tomography approach. The uplift pattern (not shown) indicates that the predictions are diminished in amplitude and the largest residuals are seen at the uplift peaks. The larger misfits in this model are due to the thicker elastic lithosphere, which was induced by the WINTERC-G temperatures (Figure 3) when translating to viscosity. As shown in Figures 5b and 5a, sharp change in viscosity occurs at a depth of ~100 km, whereas the other models show a thinner lithosphere in which this viscosity contrast occurs at 55 km. This approach results in larger lateral viscosity variations, where viscosity contrasts are up to a factor of 4.0 (compared to 2.5 obtained with the shear wave tomography approach). Nevertheless, the range in lateral viscosities here is rather narrow, in comparison to the lateral viscosity contrasts up to 10^4 found across southern British Columbia at 200 km depth (Figure 3 in Yousefi et al. (2021)).

3.5. Role of Material Compressibility

Previous models assumed incompressibility as well as laterally homogeneous viscosity. Compressibility leads to greater amplitude of predicted uplift rates in Southeast Alaska (Tanaka et al., 2015). However, differences between compressible and incompressible models can be reduced (to <10%) by adjusting the flexural rigidity of the elastic lithosphere (Tanaka et al., 2011). To isolate the role of compressibility we analyze the outcome of the best fit compressible 3-D model with its incompressible version, where the latter is obtained by adjusting Poisson's ratio to 0.4999. Note that this means that we only consider material compressibility (Klemann et al., 2003) and ignore the effects of internal buoyancy forces resulting from changes in material volume through deformation. The differences between the incompressible and compressible models can be seen in Figures 7c and 7f. The largest absolute differences, up to 5 mm/yr (~15%), are seen in GB and YK ice fields, where the largest uplift signal is seen. However, the largest percentage change in rates (20%–25%) is seen in the Southeast corner of Figures 7c and 7f, corresponding to a lower uplift signal. The

lithosphere in the compressible model can deform more easily than in the incompressible model, leading to higher peak uplift predictions.

Figure 6a includes the misfit values of a select number of incompressible models. The best fitting incompressible model has a misfit 11.7% larger than the best compressible model, so the inclusion of compressibility is an important model element. The incompressible models require a lower background viscosity than the compressible models. In other words, the compressibility weakens the material, and we need to strengthen it to achieve the same uplift rate as the incompressible model by increasing the viscosity. The best fit averaged profile (the red line in Figure 5a) shows somewhat higher viscosity values ($\sim 4.2 \times 10^{19}$ Pa-s) than the best fit model by Hu and Freymueller (2019) (3.0×10^{19} Pa-s) in the asthenosphere.

3.6. Implications for Earth Structure

Upper mantle temperatures are widely considered responsible for most seismic velocity variations in the upper mantle, whereas compositional effects are thought to have second-order effects (e.g., Cammarano et al., 2003; Goes et al., 2000). However, Goes and van der Lee (2002) also point out that the Western U.S. shows very low seismic velocities, which are likely due to fluids in the mantle introduced by the long history of subduction. In addition, Trampert and van der Hilst (2005) argue that chemical heterogeneity can introduce first-order uncertainties in the conversion from shear wave anomalies to temperature.

By using GIA and seismic tomography we were able to constrain the thermal effect on seismic velocity variations. Wang et al. (2008) showed that the thermal effects in Laurentia and Fennoscandia due to seismic anomalies are between 20% and 40%, by assuming a constant scaling factor throughout the mantle and not taking anelasticity effects into account. Wu et al. (2013) found a thermal contribution of 65% in the upper mantle, where they applied different scaling factors for the upper and lower mantle and anelasticity was taken into account.

We have found a low thermal contribution of 10% to the seismic anomalies, which implies that non-thermal effects control variations in seismic velocities. Although model misfit is similar if both background viscosity and thermal contribution are higher, such models lead to worsened fit relative to our preferred model (Figure 6a). GIA observables in Southeast Alaska are insensitive to the lower mantle structure and only weakly sensitive to deeper layers of the upper mantle (Hu & Freymueller, 2019). Therefore, it is not likely that scaling factors for deeper layers will have a large impact on our results. Uncertainty in $[\partial \ln v_s / \partial T]_{tot}$ can influence our findings. For the global averages we used Table 20.2 from Karato (2008). Uncertainties in $[\partial \ln v_s / \partial T]_{tot}$ are stated to be between 10% and 20% (Karato, 2008). Thus, the scaling factor may be underestimated between 10% and 20%. However, these uncertainties cannot explain the difference found with the global studies that found larger scaling factors.

Thus, we are left with the conclusion that non-thermal contributions to seismic velocities are large, and they are likely due to the presence of hydration and/or partial melt. If the mantle is substantially hydrated, anelastic effects would be stronger (Hyndman et al., 2009), and $[\partial \ln v_s / \partial T]_{tot}$ in Equation 1 becomes larger, which results in a larger scaling factor. Considering that the region had a long history of past subduction, it is indeed likely that the mantle is substantially hydrated (Dixon et al., 2004).

3.7. Model Limitations

There are a number of limitations to the GIA model that are briefly discussed. First of all, the uncertainties regarding the ice load model, both spatially and in time, influence the obtained earth model parameters. These uncertainties are related to both historic and PDIM load changes. The PDIM rates (1992–2012) were constrained by means of comparing GIA predictions with GPS observations in Hu and Freymueller (2019). Scaling of the ice thinning rates (Section 2.2) may not be uniform within Southeast Alaska and select areas may have an asynchronous ice load history with respect to the regional ice load model (such as YK and GB). The ice loading history was optimized for Southeast Alaska and this may not hold for all of Alaska. Moreover, the spatial loading history by Berthier et al. (2010) may be subjected to uncertainties and biases, as discussed in more detail in that study.

A second uncertainty relates to limitations in the earth model. The seismic velocity model used here (Schaeffer & Lebedev, 2013) has limited spatial resolution in this area because of the sparse station distribution. The assumptions in the seismic tomography inversion, such as model regularization, result in a very smooth model in this situation, so the details of the velocity structure are not well constrained. Regional seismic models exist (e.g., Jiang et al., 2018), but cover too small an area to have been used in this study. The lithospheric thickness was fixed for our main approach. It is possible that a good fit could be obtained for a different combination of earth model parameters, for example a larger lithosphere thickness, larger background viscosity and larger scaling factor. We investigated an alternative approach based on an olivine flow law, in which lithospheric thickness is not specified a priori and the 3-D variations are derived from a global temperature model based on seismic and gravity data. However, it resulted in worse fits compared to the scaling of seismic anomalies because it effectively imposed a lithosphere that was much too thick. This is likely due to limitations in the data used in the global WINTERC-G model. Another limitation of this alternative approach is that only diffusion creep was modeled. A number of GIA studies have shown that a power-law rheology or composite rheology improved the overall fit to GIA observables (e.g., van der Wal et al., 2013; van der Wal et al., 2010). Viscosity required for best fit cannot be reconciled with the presence of hydration or standard grain sizes. Furthermore, background stresses could be significant here and other creep mechanisms, such as grain boundary sliding and transient creep could play a role. The latter could play an important role considering the timescales of the ice history. Transient creep has been shown to play a significant role in post-seismic studies in Alaska on monthly to decadal timescales (Freed et al., 2012). However, it is unknown how transient creep will affect the modeled uplift rates given the past and current ice load changes.

4. Conclusions

In this study, the shallow upper mantle viscosity structure beneath Southeast Alaska is studied using shear wave tomography and mineral physics in a GIA model for LIA and present-day ice thickness variations. The model is constrained by GPS uplift rates. The role of thermal effects on shear wave velocity anomalies is investigated by using an adjustable scaling factor, which determines what fraction of the seismic velocity variations is due to temperature changes, as opposed to non-thermal causes. If the scaling factor is 0, then there is no thermal contribution to variations in the seismic velocity. Contrarily, a scaling factor of 1 indicates that variations in the seismic velocity are only due to thermal effects. The viscosity values are computed using a law that scales seismic velocity anomalies, and relies on a background viscosity. The scaling factor also results in lateral variations in viscosity. By using this aspect, the role of lateral viscosity variations that are expected in this tectonically active region is also investigated.

Our best fit model is obtained with a temperature scaling factor of 0.1 and background viscosity of 5.0×10^{19} Pa-s. Models with a higher background viscosity and a higher scaling factor gave similar, but worse, misfit. An acceptable range of model parameters is 0.0–0.2 for the scaling factor and $3.7\text{--}7.0 \times 10^{19}$ Pa-s, which is based on an increase of misfit within 20% which approximates a 2σ uncertainty. This result implies that the contribution of thermal effects on shear wave velocity variations is small, which implies that seismic anomalies in the shallow upper mantle are mainly controlled by non-thermal effects such as hydration and/or partial melt. The presence of hydration and/or partial melt (Dixon et al., 2004) is consistent with the tectonic history of the region. For the best fit model, the viscosities at a depth of 80 km vary between 1.9×10^{19} and 4.5×10^{19} Pa-s and viscosity variations decrease within deeper layers. The viscosities obtained here are in the same range determined by previous 1-D GIA studies focused on Southeast Alaska (Hu & Freymueller, 2019; Larsen et al., 2005; Sato et al., 2011).

To address the relevance of lateral variations in the viscosity, we have compared the 3-D results to a radially symmetric model. The 1-D viscosity profile is obtained by averaging the 3-D viscosities in each Earth layer within a predefined area. The outcome shows that the 1-D model has a slightly better fit, however, the residuals cannot be distinguished from each other within measurement uncertainties of 2σ . Therefore, we conclude that 3-D variations do not have significant impact on the predicted uplift, given the current accuracy and spatial distribution of measurements.

Our best-fit viscosities are affected by uncertainty in the ice model and earth model as discussed in Section 3.7. Knowledge of the post-LIA ice history in the region is likely better than ice history in areas subjected to GIA due to post-LGM ice melting, and large improvements from field data are not expected. However, more detailed maps of current ice changes would lead to more accurate prediction of elastic component of the uplift rate. The conclusion that 3-D viscosity does not lead to a significantly better fit is mainly dependent on the accuracy of the seismic model. Although we have used the most recent data that is suitable for our model of the study region, more seismic data or improvements in the seismic inversion would change the pattern and amplitude of the anomalies. Furthermore, the conversion of seismic velocities to viscosity introduces further uncertainty. Apart from factors such as hydration and anelasticity, variation in the parameters used to compute the viscosity anomalies in Equation 1 are possible, see for example, Ivins et al. (2021) where uncertainty from these sources for Antarctica is quantified to be up to a factor of ~ 3 (0.5 on a log-scale). Further progress in 3-D Earth rheology requires improvements in seismic models and laboratory deformation experiments to provide more accurate rheologic parametrizations that can be tested in geodynamic models.

Data Availability Statement

Input files of our FE models are available at 4TU Center for Research Data (<https://data.4tu.nl/>) under the name of this paper (<https://doi.org/10.4121/16691329>). GPS data are provided in Hu and Freymueller (2019). The shear wave velocity data we use are from the shear wave tomography model SL2013sv (Schaeffer & Lebedev, 2013). Most of the figures were prepared using Generic Mapping Tools (<https://www.generic-mapping-tools.org/>).

Acknowledgments

The authors thank an anonymous reviewer and Glenn Milne for their review and constructive suggestions which helped us to improve this manuscript. Part of this work has been done in the framework of the project “3D Earth—A Dynamic Living Planet” funded by the ESA as a Support to Science Element (STSE). This research has been partly financially supported by the GO program of the Netherlands Organization for Scientific Research (NWO), project number: ALWGO.2019.001. J. T. Freymueller was supported by the NASA, award 80NSSC17K0566.

References

- Amelung, F., & Wolf, D. (1994). Viscoelastic perturbations of the earth: Significance of the incremental gravitational force in models of glacial isostasy. *Geophysical Journal International*, 117(3), 864–879. <https://doi.org/10.1111/j.1365-246X.1994.tb02476.x>
- Argus, D. F., & Peltier, W. R. (2010). Constraining models of postglacial rebound using space geodesy: A detailed assessment of model ICE-5G (VM2) and its relatives. *Geophysical Journal International*, 181(2), 697–723. <https://doi.org/10.1111/j.1365-246X.2010.04562.x>
- Artemieva, I. M., Billien, M., L  v  que, J.-J., & Mooney, W. D. (2004). Shear wave velocity, seismic attenuation, and thermal structure of the continental upper mantle. *Geophysical Journal International*, 157(2), 607–628. <https://doi.org/10.1111/j.1365-246X.2004.02195.x>
- Barnhoorn, A., van der Wal, W., & Drury, M. R. (2011). Upper mantle viscosity and lithospheric thickness under Iceland. *Journal of Geodynamics*, 52(3), 260–270. <https://doi.org/10.1016/j.jog.2011.01.002>
- Berthier, E., Schiefer, E., Clarke, G. K. C., Menounos, B., & R  my, F. (2010). Contribution of Alaskan glaciers to sea level rise derived from satellite imagery. *Nature Geoscience*, 3(2), 92–95. <https://doi.org/10.1038/ngeo737>
- Cammarano, F., Goes, S., Vacher, P., & Giardini, D. (2003). Inferring upper-mantle temperatures from seismic velocities. *Physics of the Earth and Planetary Interiors*, 138(3), 197–222. [https://doi.org/10.1016/S0031-9201\(03\)00156-0](https://doi.org/10.1016/S0031-9201(03)00156-0)
- DeMets, C., & Merkuriev, S. (2016). High-resolution reconstructions of Pacific–North America plate motion: 20 Ma to present. *Geophysical Journal International*, 207(2), 741–773. <https://doi.org/10.1093/gji/ggw305>
- Dixon, J. E., Dixon, T. H., Bell, D. R., & Malservisi, R. (2004). Lateral variation in upper mantle viscosity: Role of water. *Earth and Planetary Science Letters*, 222(2), 451–467. <https://doi.org/10.1016/j.epsl.2004.03.022>
- Durkin, W., Kachuck, S., & Pritchard, M. (2019). The importance of the inelastic and elastic structures of the crust in constraining glacial density, mass change, and isostatic adjustment from geodetic observations in Southeast Alaska. *Journal of Geophysical Research: Solid Earth*, 124(1), 1106–1119. <https://doi.org/10.1029/2018JB016399>
- Dziewonski, A. M., & Anderson, D. L. (1981). Preliminary reference Earth model. *Physics of the Earth and Planetary Interiors*, 25(4), 297–356. [https://doi.org/10.1016/0031-9201\(81\)90046-7](https://doi.org/10.1016/0031-9201(81)90046-7)
- Elliott, J. L., Larsen, C. F., Freymueller, J. T., & Motyka, R. J. (2010). Tectonic block motion and glacial isostatic adjustment in Southeast Alaska and adjacent Canada constrained by GPS measurements. *Journal of Geophysical Research*, 115(B9). <https://doi.org/10.1029/2009JB007139>
- Engelbreton, D. C., Cox, A., & Gordon, R. G. (1984). Relative motions between oceanic plates of the Pacific Basin. *Journal of Geophysical Research*, 89(B12), 10291–10310. <https://doi.org/10.1029/JB089iB12p10291>
- Freed, A. M., Hirth, G., & Behn, M. D. (2012). Using short-term postseismic displacements to infer the ambient deformation conditions of the upper mantle. *Journal of Geophysical Research*, 117(B1). <https://doi.org/10.1029/2011JB008562>
- Fullea, J., Lebedev, S., Martinec, Z., & Celli, N. L. (2021). WINTERC-G: Mapping the upper mantle thermochemical heterogeneity from coupled geophysical–petrological inversion of seismic waveforms, heat flow, surface elevation and gravity satellite data. *Geophysical Journal International*, 226(1), 146–191. <https://doi.org/10.1093/gji/ggab094>
- Fuston, S., & Wu, J. (2020). Raising the resurrection plate from an unfolded-slab plate tectonic reconstruction of northwestern North America since early Cenozoic time. *Geological Society of America Bulletin*, 133, 1128, 1140. <https://doi.org/10.1130/B35677.1>
- Goes, S., Govers, R., & Vacher, P. (2000). Shallow mantle temperatures under Europe from P and S wave tomography. *Journal of Geophysical Research*, 105(B5), 11153–11169. <https://doi.org/10.1029/1999JB900300>
- Goes, S., & van der Lee, S. (2002). Thermal structure of the North American uppermost mantle inferred from seismic tomography. *Journal of Geophysical Research*, 107(B3), ETG 2-1–ETG 2-13. <https://doi.org/10.1029/2000JB000049>

- Haeussler, P. J., Bradley, D. C., Wells, R. E., & Miller, M. L. (2003). Life and death of the resurrection plate: Evidence for its existence and subduction in the northeastern Pacific in Paleocene-Eocene time. *Geological Society of America Bulletin*, 115(7), 867–880. [https://doi.org/10.1130/0016-7606\(2003\)115<0867:LADOTR>2.0.CO;2](https://doi.org/10.1130/0016-7606(2003)115<0867:LADOTR>2.0.CO;2)
- Hibbitt, D., Karlsson, B., & Sorensen, P. (2016). *Getting started with ABAQUS, version (6.14)*. Hibbitt, Karlsson & Sorensen, Inc.
- Hirth, G., & Kohlstedt, D. (2003). Rheology of the upper mantle and the mantle wedge: A view from the experimentalists. In *Inside the subduction factory* (pp. 83–105).
- Hu, Y., & Freymueller, J. T. (2019). Geodetic observations of time-variable glacial isostatic adjustment in Southeast Alaska and its implications for Earth rheology. *Journal of Geophysical Research: Solid Earth*, 124(9), 9870–9889. <https://doi.org/10.1029/2018JB017028>
- Hyndman, R. D. (2017). Lower-crustal flow and detachment in the North American Cordillera: A consequence of Cordillera-wide high temperatures. *Geophysical Journal International*, 209(3), 1779–1799. <https://doi.org/10.1093/gji/ggx138>
- Hyndman, R. D., Currie, C. A., Mazzotti, S., & Frederiksen, A. (2009). Temperature control of continental lithosphere elastic thickness, Te vs Vs. *Earth and Planetary Science Letters*, 277(3), 539–548. <https://doi.org/10.1016/j.epsl.2008.11.023>
- Ivins, E. R., & Sammis, E. G. (1995). On lateral viscosity contrast in the mantle and the rheology of low-frequency geodynamics. *Geophysical Journal International*, 123(2), 305–322. <https://doi.org/10.1111/j.1365-246X.1995.tb06856.x>
- Ivins, E. R., van der Wal, W., Wiens, D. A., Lloyd, A., & Caron, L. (2021). Antarctic upper mantle rheology. In *The geochemistry and geophysics of the Antarctic mantle* (Vol. 56). Geological Society, London, Memoirs, in press. <https://doi.org/10.1144/m56-2020-19>
- James, T. S., Gowan, E. J., Wada, I., & Wang, K. (2009). Viscosity of the asthenosphere from glacial isostatic adjustment and subduction dynamics at the northern Cascadia subduction zone, British Columbia, Canada. *Journal of Geophysical Research*, 114(B4). <https://doi.org/10.1029/2008JB006077>
- Jiang, C., Schmandt, B., Ward, K. M., Lin, F.-C., & Worthington, L. L. (2018). Upper mantle seismic structure of Alaska from Rayleigh and S Wave Tomography. *Geophysical Research Letters*, 45(19), 10350–10359. <https://doi.org/10.1029/2018GL079406>
- Karato, S. (2008). *Deformation of earth materials: An introduction to the rheology of solid*. Cambridge University Press.
- Klemann, V., Wu, P., & Wolf, D. (2003). Compressible viscoelasticity: Stability of solutions for homogeneous plane-Earth models. *Geophysical Journal International*, 153(3), 569–585. <https://doi.org/10.1046/j.1365-246X.2003.01920.x>
- Koehler, R. D. (2013). *Quaternary Faults and Folds (QFF)*. Alaska Division of Geological & Geophysical Surveys Digital Data Series 3. <https://doi.org/10.14509/24956>
- Larsen, C. F., Motyka, R. J., Arendt, A. A., Echelmeyer, K. A., & Geissler, P. E. (2007). Glacier changes in Southeast Alaska and northwest British Columbia and contribution to sea level rise. *Journal of Geophysical Research*, 112(1). <https://doi.org/10.1029/2006JF000586>
- Larsen, C. F., Motyka, R. J., Freymueller, J. T., Echelmeyer, K. A., & Ivins, E. R. (2005). Rapid viscoelastic uplift in Southeast Alaska caused by post-Little Ice Age glacial retreat. *Earth and Planetary Science Letters*, 237(3), 548–560. <https://doi.org/10.1016/j.epsl.2005.06.032>
- Li, T., Wu, P., Wang, H., Steffen, H., Khan, N. S., Engelhart, S. E., et al. (2020). Uncertainties of glacial isostatic adjustment model predictions in North America associated with 3d structure. *Geophysical Research Letters*, 47(10), e2020GL087944. <https://doi.org/10.1029/2020GL087944>
- Pasyanos, M. E., Masters, T. G., Laske, G., & Ma, Z. (2014). LITHO1.0: An updated crust and lithospheric model of the Earth. *Journal of Geophysical Research: Solid Earth*, 119(3), 2153–2173. <https://doi.org/10.1002/2013JB010626>
- Peltier, W. R. (2004). Global glacial isostasy and the surface of the Ice-Age Earth: The ICE-5G (VM2) model and GRACE. *Annual Review of Earth and Planetary Sciences*, 32(1), 111–149. <https://doi.org/10.1146/annurev.earth.32.082503.144359>
- Peltier, W. R., Argus, D. F., & Drummond, R. (2015). Space geodesy constrains ice age terminal deglaciation: The global ICE-6G_C (VM5a) model. *Journal of Geophysical Research: Solid Earth*, 120(1), 450–487. <https://doi.org/10.1002/2014JB011176>
- Sabadini, R., Yuen, D. A., & Boschi, E. (1982). Polar wandering and the forced responses of a rotating, multilayered, viscoelastic planet. *Journal of Geophysical Research*, 87(B4), 2885–2903. <https://doi.org/10.1029/JB087iB04p02885>
- Sato, T., Larsen, C. F., Miura, S., Ohta, Y., Fujimoto, H., Sun, W., et al. (2011). Reevaluation of the viscoelastic and elastic responses to the past and present-day ice changes in Southeast Alaska. *Tectonophysics*, 511(3), 79–88. <https://doi.org/10.1016/j.tecto.2010.05.009>
- Schaeffer, A. J., & Lebedev, S. (2013). Global shear speed structure of the upper mantle and transition zone. *Geophysical Journal International*, 194(1), 417–449. <https://doi.org/10.1093/gji/ggt095>
- Schotman, H. H. A., Vermeersen, L. L. A., Wu, P., Drury, M. R., & De Bresser, J. H. P. (2009). Constraints on shallow low-viscosity zones in Northern Europe from future GOCE gravity data. *Geophysical Journal International*, 178(1), 65–84. <https://doi.org/10.1111/j.1365-246X.2009.04160.x>
- Schotman, H. H. A., Wu, P., & Vermeersen, L. L. A. (2008). Regional perturbations in a global background model of glacial isostasy. *Physics of the Earth and Planetary Interiors*, 171(1), 323–335. <https://doi.org/10.1016/j.pepi.2008.02.010>
- Smith-Konter, B. R., Thornton, G. M., & Sandwell, D. T. (2014). Vertical crustal displacement due to interseismic deformation along the San Andreas Fault: Constraints from tide gauges. *Geophysical Research Letters*, 41(11), 3793–3801. <https://doi.org/10.1002/2014GL060091>
- Spada, G. (2003). *The theory behind TABOO*. Samizdat Press.
- Spada, G., Antonioli, A., Boschi, L., Brandi, V., Cianetti, S., Galvani, G., et al. (2003). *TABOO, user guide*. Samizdat Press.
- Spada, G., Antonioli, A., Cianetti, S., & Giunchi, C. (2006). Glacial isostatic adjustment and relative sea-level changes: The role of lithospheric and upper mantle heterogeneities in a 3-D spherical Earth. *Geophysical Journal International*, 165(2), 692–702. <https://doi.org/10.1111/j.1365-246X.2006.02969.x>
- Spada, G., Barletta, V. R., Klemann, V., Riva, R. E. M., Martinec, Z., Gasperini, P., et al. (2011). A benchmark study for glacial isostatic adjustment codes. *Geophysical Journal International*, 185(1), 106–132. <https://doi.org/10.1111/j.1365-246X.2011.04952.x>
- Stacey, F., & Davis, P. (2008). *Physics of the Earth*. Cambridge University Press.
- Tanaka, Y., Klemann, V., Martinec, Z., & Riva, R. E. M. (2011). Spectral-finite element approach to viscoelastic relaxation in a spherical compressible Earth: Application to GIA modelling. *Geophysical Journal International*, 184(1), 220–234. <https://doi.org/10.1111/j.1365-246X.2010.04854.x>
- Tanaka, Y., Sato, T., Ohta, Y., Miura, S., Freymueller, J. T., & Klemann, V. (2015). The effects of compressibility on the GIA in Southeast Alaska. *Journal of Geodynamics*, 84, 55–61. <https://doi.org/10.1016/j.jog.2014.10.001>
- Trampert, J., & van der Hilst, R. D. (2005). Towards a quantitative interpretation of global seismic tomography. *Geophysical Monograph Series*, 160, 47–62. <https://doi.org/10.1029/160gm05>
- van der Wal, W., Barnhoorn, A., Stocchi, P., Gradmann, S., Wu, P., Drury, M., & Vermeersen, B. (2013). Glacial isostatic adjustment model with composite 3-D Earth rheology for Fennoscandia. *Geophysical Journal International*, 194(1), 61–77. <https://doi.org/10.1093/gji/ggt099>
- van der Wal, W., Wu, P., Wang, H., & Sideris, M. G. (2010). Sea levels and uplift rate from composite rheology in glacial isostatic adjustment modeling. *Journal of Geodynamics*, 50(1), 38–48. <https://doi.org/10.1016/j.jog.2010.01.006>

- Wang, H., Wu, P., & van der Wal, W. (2008). Using postglacial sea level, crustal velocities and gravity-rate-of-change to constrain the influence of thermal effects on mantle lateral heterogeneities. *Journal of Geodynamics*, 46, 104–117. <https://doi.org/10.1016/j.jog.2008.03.003>
- Wheeler, L. B. (2013). *Modeling the influence of the last glacial maximum ice load on the tectonics of Southeast Alaska and the South Island, New Zealand* (Electronic Theses and Dissertations, 2043). University of Maine. Retrieved from <https://digitalcommons.library.umaine.edu/etd/2043/>
- Wu, P. (2004). Using commercial finite element packages for the study of Earth deformations, sea levels and the state of stress. *Geophysical Journal International*, 158(2), 401–408. <https://doi.org/10.1111/j.1365-246X.2004.02338.x>
- Wu, P., & Johnston, P. (1998). Validity of using flat-earth finite element models in the study of postglacial rebound. In P. Wu (Ed.), *Dynamics of the ice age Earth* (pp. 191–202). Trans Tech Publications Ltd.
- Wu, P., Wang, H., & Steffen, H. (2013). The role of thermal effect on mantle seismic anomalies under Laurentia and Fennoscandia from observations of Glacial Isostatic Adjustment. *Geophysical Journal International*, 192. <https://doi.org/10.1093/gji/ggs009>
- Yousefi, M., Milne, G. A., & Latychev, K. (2021). Glacial isostatic adjustment of the Pacific Coast of North America: The influence of lateral Earth structure. *Geophysical Journal International*, 226(1), 91–113. <https://doi.org/10.1093/gji/ggab053>

References From the Supporting Information

- Behn, M., Hirth, G., & Elsenbeck, J. (2008). Implications of grain size evolution on the seismic structure of the oceanic upper mantle. *Earth and Planetary Science Letters*, 282, 178–189. <https://doi.org/10.1016/j.epsl.2009.03.014>
- Behn, M. D., Hirth, G., & Elsenbeck, J. R. (2009). Implications of grain size evolution on the seismic structure of the oceanic upper mantle. *Earth and Planetary Science Letters*, 282(1), 178–189. <https://doi.org/10.1016/j.epsl.2009.03.014>
- Bell, D. R., Rossman, G. R., Maldener, J., Endisch, D., & Rauch, F. (2003). Hydroxide in olivine: A quantitative determination of the absolute amount and calibration of the IR spectrum. *Journal of Geophysical Research*, 108(B2). <https://doi.org/10.1029/2001JB000679>
- Dixon, J. E., Dixon, T. H., Bell, D. R., & Malservisi, R. (2004). Lateral variation in upper mantle viscosity: Role of water. *Earth and Planetary Science Letters*, 222(2), 451–467. <https://doi.org/10.1016/j.epsl.2004.03.022>
- Freed, A. M., Hirth, G., & Behn, M. D. (2012). Using short-term postseismic displacements to infer the ambient deformation conditions of the upper mantle. *Journal of Geophysical Research*, 117(B1). <https://doi.org/10.1029/2011JB008562>
- Fullea, J., Lebedev, S., Martinec, Z., & Celli, N. L. (2021). WINTERC-G: Mapping the upper mantle thermochemical heterogeneity from coupled geophysical–petrological inversion of seismic waveforms, heat flow, surface elevation and gravity satellite data. *Geophysical Journal International*, 226(1), 146–191. <https://doi.org/10.1093/gji/ggab094>
- Goes, S., Govers, R., & Vacher, P. (2000). Shallow mantle temperatures under Europe from P and S wave tomography. *Journal of Geophysical Research*, 105(B5), 11153–11169. <https://doi.org/10.1029/1999JB900300>
- Himmelberg, G., & Loney, R. (1986). *Characteristics and petrogenesis of Alaskan-type ultramafic-mafic intrusions*. U.S. Geological Survey Professional Paper, 1564.
- Himmelberg, G., Loney, R., & Craig, J. (1986). *Petrogenesis of the ultramafic complex at the Blashke Islands, Southeastern Alaska*. U.S. Geological Survey Bulletin, 1662.
- Hirth, G., & Kohlstedt, D. (2003). Rheology of the upper mantle and the mantle wedge: A view from the experimentalists. In *Inside the subduction factory* (pp. 83–105).
- Hu, Y., & Freymueller, J. T. (2019). Geodetic observations of time-variable glacial isostatic adjustment in Southeast Alaska and its implications for Earth rheology. *Journal of Geophysical Research: Solid Earth*, 124(9), 9870–9889. <https://doi.org/10.1029/2018JB017028>
- Hyndman, R. D. (2017). Lower-crustal flow and detachment in the North American Cordillera: A consequence of Cordillera-wide high temperatures. *Geophysical Journal International*, 209(3), 1779–1799. <https://doi.org/10.1093/gji/ggx138>
- Hyndman, R. D., Currie, C. A., Mazzotti, S., & Frederiksen, A. (2009). Temperature control of continental lithosphere elastic thickness, Te vs Vs. *Earth and Planetary Science Letters*, 277(3), 539–548. <https://doi.org/10.1016/j.epsl.2008.11.023>
- Larsen, C. F., Motyka, R. J., Freymueller, J. T., Echelmeyer, K. A., & Ivins, E. R. (2005). Rapid viscoelastic uplift in Southeast Alaska caused by post-Little Ice Age glacial retreat. *Earth and Planetary Science Letters*, 237(3), 548–560. <https://doi.org/10.1016/j.epsl.2005.06.032>
- Morales, L. F. G., & Tommasi, A. (2011). Composition, textures, seismic and thermal anisotropies of xenoliths from a thin and hot lithospheric mantle (Summit Lake, southern Canadian Cordillera). *Tectonophysics*, 507(1), 1–15. <https://doi.org/10.1016/j.tecto.2011.04.014>
- Schmidt, P. (2012). *Glacial isostatic adjustment: Inferences on properties and processes in the upper mantle from 3D dynamical modeling*. Uppsala University, Disciplinary Domain of Science and Technology, Earth Sciences, Department of Earth Sciences, Geophysics.
- Stacey, F., & Davis, P. (2008). *Physics of the Earth*. Cambridge University Press.
- Turcotte, D., & Schubert, G. (2002). *Geodynamics*. Cambridge University Press.
- van der Lee, S., & Frederiksen, A. (2005). Surface wave tomography applied to the North American upper mantle. In *Seismic Earth: Array analysis of broadband seismograms* (pp. 67–80).
- van der Wal, W., Barnhoorn, A., Stocchi, P., Gradmann, S., Wu, P., Drury, M., & Vermeersen, B. (2013). Glacial isostatic adjustment model with composite 3-D Earth rheology for Fennoscandia. *Geophysical Journal International*, 194(1), 61–77. <https://doi.org/10.1093/gji/ggt099>
- Whitehouse, P. L. (2018). Glacial isostatic adjustment modelling: Historical perspectives, recent advances, and future directions. *Earth Surface Dynamics*, 6(2), 401–429. <https://doi.org/10.5194/esurf-6-401-2018>